

Cite this: DOI: 10.1039/xxxxxxxxxx

Three-dimensional atomic models from a single Z-contrast image: verification by electron tomography and opportunities [†]

A. De Backer,^a L. Jones,^b I. Lobato,^a T. Altantzis,^a B. Goris,^a P.D. Nellist,^b S. Bals,^{*a} and S. Van Aert^{*a}

Received Date

Accepted Date

DOI: 10.1039/xxxxxxxxxx

www.rsc.org/journalname

In order to fully exploit structure-property relations of nanomaterials, three-dimensional (3D) characterization at the atomic scale is often required. In recent years, the resolution of electron tomography has reached the atomic scale. However, such tomography typically requires several projection images demanding substantial electron dose. A newly developed alternative circumvents this by counting the number of atoms across a single projection image. These atom counts can be used to create an initial atomic model with which an energy minimization can be applied to obtain a relaxed 3D reconstruction of the nanoparticle. Here, we compare, at the atomic scale, this single image reconstruction approach with tomography and find an excellent agreement. This new approach allows for the characterization of beam-sensitive materials, or where the acquisition of a tilt series is impossible. As an example, the utility is illustrated by the 3D atomic scale characterization of a nanodumbbell on an *in situ* heating holder of limited tilt range.

Introduction

Modern experimental characterization techniques should be able to determine the structure of nanoparticles at the atomic scale, since the particle's properties are directly related to the atomic structure. Scanning transmission electron microscopy (STEM) is established as a valuable method to investigate nanomaterials. However, two-dimensional (2D) projection images may result in an incomplete characterization of the material's structure. Therefore, different techniques to retrieve the three-dimensional (3D) atomic structure have been suggested in the field of electron microscopy. One of the most well known and promising techniques to achieve atomic resolution in 3D is electron tomography^{1,2}. For this, a series of 2D projection images at different tilt angles is used as an input for a computer algorithm to obtain a 3D reconstruction. Although this is not yet routinely possible for all structures, the scope of electron tomography has been pushed beyond 3D characterization at the nanoscale in order to also resolve atomic positions in 3D. Van Aert et al. demonstrated the visualization of individual atoms for the first time in 3D from 2D projection images using discrete tomography³. The same approach

has been used to reconstruct the core of a PbSe-CdSe nanoparticle⁴. Shortly after, a reconstruction technique based on compressive sensing was developed for a 3D reconstruction at the atomic scale. This technique has successfully been applied at the atomic scale using annular dark field (ADF) STEM for the determination of surface facets in Au nanorods⁵. Recently, lattice strain measurement was demonstrated in 3D using a model-based electron tomography technique⁶ or by using a reconstruction technique known as equal sloped tomography⁷. Furthermore, 3D reconstruction methods are evolving toward unscrambling mixed elements at the atomic scale^{8–10}. However, for a successful 3D reconstruction using electron tomography, there are several limitations. Electron tomography requires multiple exposures which is not always feasible in practice. For example, *in situ* experiments or the characterization of beam sensitive materials at the atomic scale are nearly impossible using electron tomography. In order to overcome these limitations, alternatives to electron tomography for a 3D reconstruction at the atomic scale have been proposed where the 3D atomic structure is reconstructed from a single image^{9,11–14}. The alternative method considered here^{11,13} combines atom-counting in ADF STEM^{15–18} with prior knowledge about a material's crystal structure. An energy minimization using ab-initio calculations or a Monte Carlo approach is then performed to relax the nanoparticle's 3D structure. The latter approach was recently applied to study oriented attachment in a 2D lattice of PbSe quantum dots which was extremely sensitive to the electron beam¹⁹.

^a Electron Microscopy for Materials Research (EMAT), University of Antwerp, Groenenborgerlaan 171, B-2020 Antwerp, Belgium

^b Department of Materials, University of Oxford, OX13PH Oxford, United Kingdom

* Corresponding authors: sandra.vanaert@uantwerpen.be, sara.bals@uantwerpen.be

[†] Electronic Supplementary Information (ESI) available: [details of any supplementary information available should be included here]. See DOI: 10.1039/b000000x/

In this paper, we begin by validating our new atom-counting/energy-minimization approach against state-of-the-art compressive sensing electron tomography; first at room temperature using a high tilt tomography holder. Once validated, we exploit this with the single viewing direction available from an *in situ* heating holder. The retrieved 3D atomic reconstructions directly reveal changes in facet-type and facet-area ratio's. We expect these measured properties to be of critical importance for the study of catalysis^{5,20–23}.

Experimental details & Methods

Electron microscopy

Au nanorods and nanodumbbells were grown in the BioNanoPlasmonics Lab in Spain, following the procedure previously reported by Grzelczak and co-workers²⁴. ADF STEM projection images were acquired using an aberration corrected FEI-Titan cubed 60–300 electron microscope. The electron microscope was operated at 200 keV with a 24 mrad convergence angle for imaging the Au nanorod for the validation against electron tomography and operated at 300 keV with a 21.4 mrad convergence angle for imaging the Au nanodumbbell on the *in situ* heating holder. The inner and outer detector collection angles were 45 mrad and 160 mrad respectively. For the acquisition of low and high magnification tomography series, a Fischione model 2040 tilt-rotation tomography holder was used. The low magnification series were acquired within a tilt range from -70° to $+70^\circ$ and a tilt increment of 5° . The high resolution reconstruction was obtained by minimizing the $L1$ norm of the object simultaneously with the projection distance, as explained in Ref.⁵. For the acquisition of the high resolution projection images of the Au dumbbell before and after heating, a GATAN double-tilt-*in situ* holder was used. During this experiment, a series of 16 images of 1024×1024 pixels with a dwell time of $2 \mu\text{s}$ per pixel were recorded in quick succession to minimize sample damage and counter non-linear distortions. The effects of linear scan-drift were minimized by incorporating a 90° scan-rotation between the successive frames²⁵. The image series was rigid aligned to counter stage-drift, and then non-rigid registered to counter non-linear environmental distortion using the SmartAlign software²⁶.

Atom-counting

For each of the projection images, the number of atoms in the projected atomic columns was determined using a statistics-based atom-counting method^{16–18}. The atom-counting was performed using StatSTEM²⁷. This statistics-based method relies on an atomic column by atomic column quantification of the so-called scattering cross-sections^{28,29}, i.e. the total intensity of scattered electrons for each projected atomic column. To achieve this, the image is first modeled by a superposition of Gaussian peaks located at the atomic column positions^{27,30}. The scattering cross-section equals the volume under the Gaussian peak and can be calculated for each projected atomic column. Next, the distribution of scattering cross-sections from all the atomic columns is decomposed into overlapping normal distributions, where the number of normal components is selected using an integrated

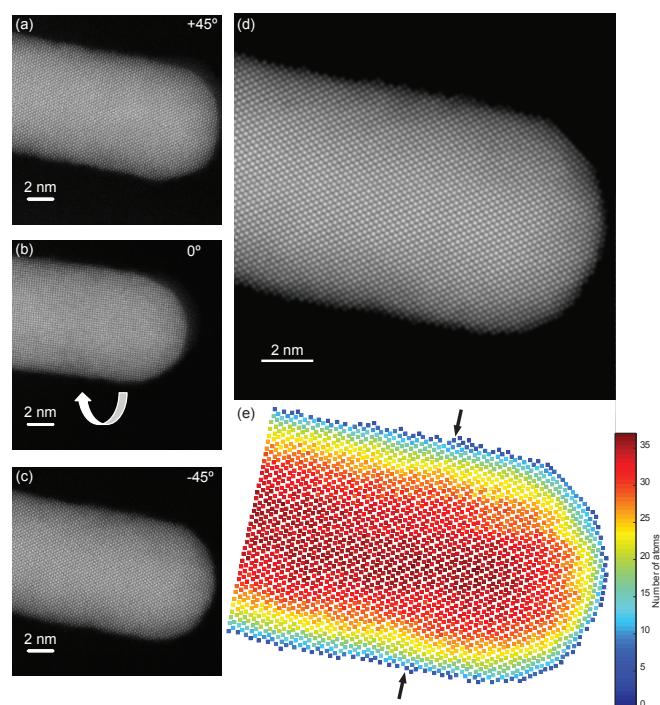


Fig. 1 High resolution ADF STEM projection images of a Au nanorod and statistical atom-counting (a,b,c) Three projection images obtained by tilting the nanorod around the long axis. (d) Refined model of projection image (c). (e) Atom-counts for this projection image.

classification likelihood approach. The number of atoms in each projected atomic column is then obtained by assigning the component that generates the experimental scattering cross-section with the highest probability. This results in a map with the atom-counts in each projected atomic column.

Energy minimization

Based on the atom-counting results, an initial 3D configuration can be obtained by positioning the atoms in each atomic column, parallel to the beam direction, symmetrically around a central plane. The atoms are separated by a fixed distance a or $a/\sqrt{2}$ for the $[100]$ and $[110]$ orientation respectively (where $a = 4.078 \text{ \AA}$ is the lattice parameter of gold). In addition, prior knowledge about the $[100]$ or $[110]$ specimen orientation can be included. For example, for the $[110]$ orientation the atomic position at even planes are shifted along the beam direction by $a/(2\sqrt{2})$ with respect to the odd planes. The relative heights of the atomic columns are then relaxed using a Monte Carlo approach using a Lennard-Jones potential¹³. Since the number of atoms in each column is determined by the earlier atom-counting analysis and since the atoms are not permitted to move between columns, this relaxation is more computationally efficient than approaches needing to solve both the atom-counts and heights simultaneously¹⁴. For the *in situ* heating of the Au nanoparticle, the surface facets are of special interest. However, the energy minimization method described by Jones et al.¹³ reconstructs the general morphology using an easily calculated, but somewhat simplified, Lennard-Jones

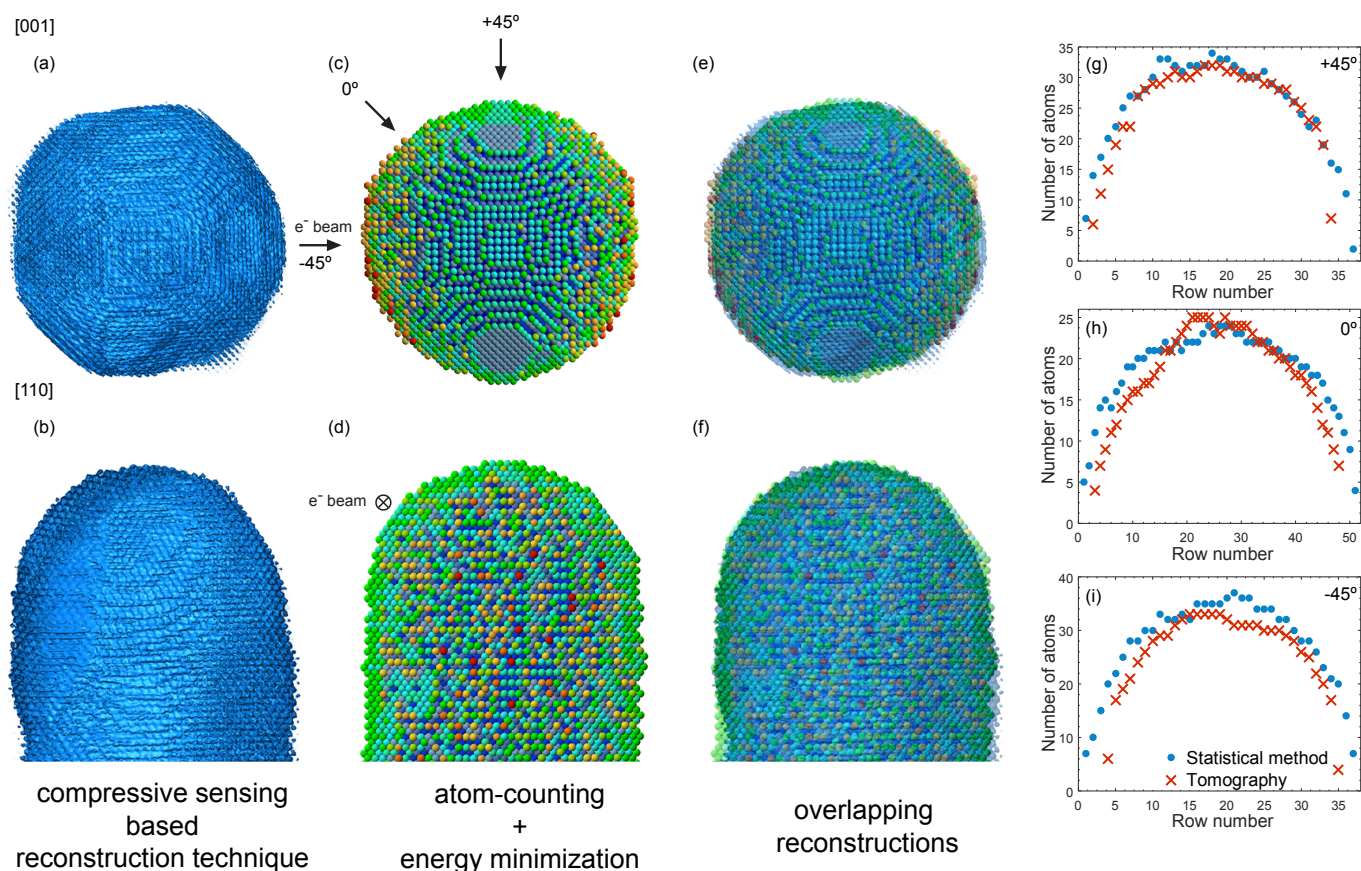


Fig. 2 Comparison of the reconstructions based on atom-counting with energy minimization and those obtained by atomic resolution tomography (a,b) Compressive sensing based reconstruction of Au nanorod viewed along [001] and [110] direction. (c,d) Reconstruction based on atom-counting and energy minimization using a single projection image (Fig. 1(a)) viewed along [001] and [110] orientation (the coloring of the Au atoms indicates the nearest-neighbor coordination, from 1 in red to 12 in dark blue). (e,f) Overlap of reconstructions shown in (a,c) and (b,d). (g,h,i) Comparison of atom-counts along different orientations from an orthogonal slice from the compressive sensing based reconstruction (red crosses) and statistical atom-counting results obtained from the three ADF STEM images of Fig. 1 (a-c) (blue dots).

potential. This simplified potential may not capture the full free-energy behavior at the surfaces and may not reconstruct details on the surface facets for particles containing more than a few thousand atoms. Therefore, more complete molecular dynamics (MD) simulations employing the gold embedded atom method (EAM) potential³¹ have been performed using the GPU LAMMPS package for the relaxation of the initial 3D models for the heating experiment^{32,33}. First, the initial 3D models of the nanodumbbell and nanorod, which contain 10^6 atoms were structurally relaxed by minimizing the energy of the system at $T = 0$ K in order to reduce the stress in the system. Then a full MD relaxation was performed in the canonical ensemble with a time step of 3 fs, an equilibration period of 15 ns, and a production of 3 ns. Over the production time each atomic position has been extracted every 6 fs step. The MD simulation has been carried out for a large cubic box without periodic boundary conditions so that the surface of the nanorod is free. In this MD approach, atoms are allowed to move between columns. This is justified because of the limited precision of the atom-counts, introduced by the electron counting noise, scan noise, and other instrumental limitations^{16,26,34,35}.

Results & Discussion

Electron tomography versus atom-counting combined with energy minimization

Three projection ADF STEM images of a Au nanorod were acquired along different major zone axes. The experimental images are shown in Fig. 1(a-c). For each of the projection images, the number of atoms in the projected atomic columns was determined using the statistics-based atom-counting method^{16,17}. Drift corrected images were modeled as a superposition of Gaussian functions using StatSTEM²⁷, details about the correction can be found in Section S1 of the Electronic Supplementary Information. In Fig. 1(d), the refined model is shown for the drift corrected image of the projection image shown in Fig. 1(c). The resulting atom-counting map is shown in Fig. 1(e). More details on the atom-counting analysis for the three atomic resolution images in Fig. 1 can be found in the Electronic Supplementary Information, Section S2 and Figs. S1-S3. Based on the counting results, an initial symmetrical 3D atomic resolution model was built which is then relaxed by minimizing its energy. In parallel, the three projection images of Fig. 1(a-c) were used as an input for a 3D reconstruction using a compressive sensing based recon-

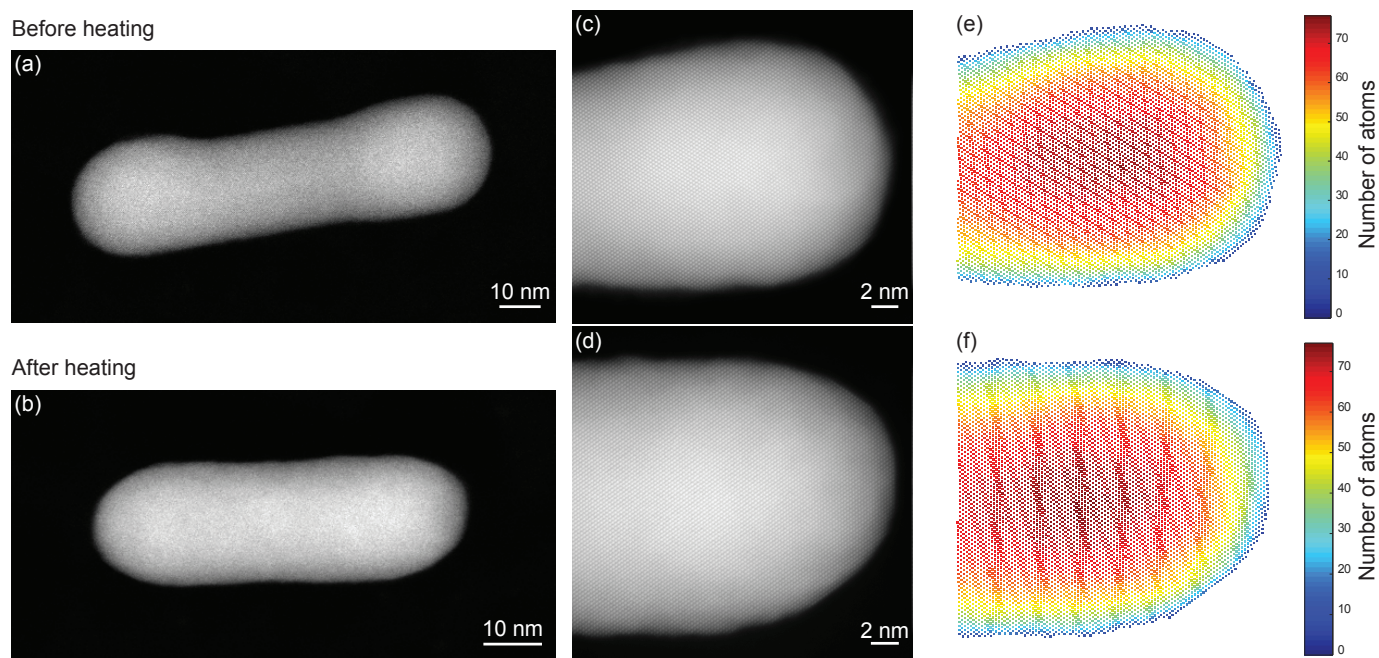


Fig. 3 Heating experiment (a,b) Overview image of Au dumbbell/rod before and after heating. (c,d) SmartAlign distortion corrected average of the Au dumbbell/rod before and after heating. (e,f) Atom-counts before and after heating.

struction technique⁵. For a 3D reconstruction at the atomic scale, the sparsity of the object can be exploited in the reconstruction algorithm, as only a limited number of voxels contains an atom and most voxels correspond to vacuum.

In Fig. 2, a comparison is shown between the two atomic resolution reconstruction methods. Unlike the compressive sensing based reconstruction, the reconstruction using atom-counting combined with energy minimization is based on a single projection image, which is here the projection image recorded at -45° . Similar 3D atomic models are expected when performing atom-counting and energy minimization starting from the two other projection images ($+45^\circ$ and 0° , Figs. 1(a) and (b), respectively). Fig. 2(a,b) show the compressive sensing based reconstruction visualized along the [001] and [110] directions respectively, and similarly Fig. 2(c,d) show the reconstruction based on the atom-counting/energy-minimization approach. Both reconstructions are overlapped in Fig. 2(e,f) and an excellent visual match of the overall morphology of the nanorod has been found. This agreement is only made possible because of the high accuracy of the statistically determined atom-counts. In order to compare the atom-counting results with the atomic-resolution compressive sensing based reconstruction in a more quantitative manner, the obtained atom counts from each projection image in Fig. 1(a-c) are compared with the number of atoms that can be extracted from different directions from an orthogonal slice of the atomic resolution compressive sensing based reconstruction. This comparison is illustrated in Fig. 2(g-i). The number of atoms has been counted in the 40th atomic plane from the tip of the Au nanorod, which is arrowed in Fig. 1(e). Good agreement between the counts derived from the 3D reconstruction and from the statistics-based atom-counting method is obtained.

Slight deviations can be expected, since the tomographic reconstruction represents the average structure based on the three high-resolution projection images, whereas the atom-counts result from each image separately. While the accuracy is neatly verified, factors affecting the precision of these counts have been discussed elsewhere previously^{16,26,34–36}. The comparison between the atom-counting/energy-minimization approach and state-of-the-art electron tomography validates that a trustworthy 3D reconstruction can be obtained from a single image, where we can make reasonable assumptions that we are viewing a roughly symmetrical particle with no voids. Atom-counting combined with energy minimization now opens up new possibilities for the 3D characterization of materials where electron tomography cannot be applied. Perhaps the biggest potential scope for this is where *in situ* holders simply do not exist with sufficient tilt ranges for tomography. Here, we illustrate the utility of the proposed approach for imaging a Au nanodumbbell on an *in situ* heating holder.

Heating experiment

In this experiment we evaluate the structure of a Au nanodumbbell before and after heating. We deploy the atom-counting/energy-minimization approach discussed above, to estimate a 3D atomic model from a single 2D image, since the heating holder does not allow sufficient tilt for tomography. Fig. 3(a) shows an overview image of the nanodumbbell prior to heating. A higher resolution image of the right part is depicted in Fig. 3(c). Next, the Au nanodumbbell was heated up to 330°C . The temperature was ramped up to 100°C , 200°C , 275°C and 330°C , and was maintained for 5 minutes at each acquired stage. After heating, the sample was allowed to cool to room temperature in vacuum to investigate structural changes at

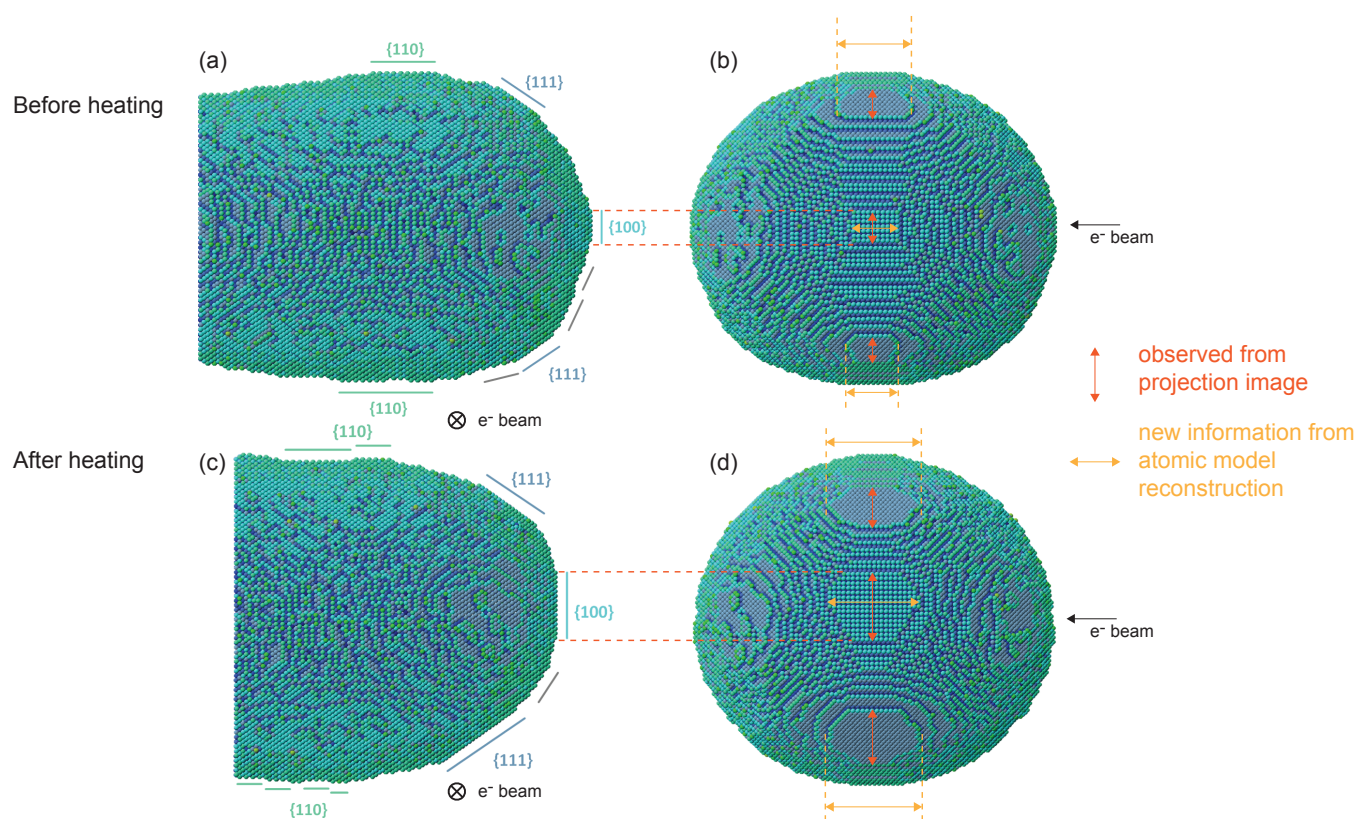


Fig. 4 Three-dimensional atomic resolution reconstructions of the nanodumbbell/nanorod used for the heating experiment along different viewing directions (a,b) Au dumbbell before heating, (c,d) Au rod after heating. The coloring of the Au atoms determines the nearest-neighbor coordination.

high resolution. An overview image (Fig. 3(b)) and an atomic resolution image of the right part (Fig. 3(d)) were again acquired along a single orientation. From the overview images, it is clear that the nanodumbbell underwent a morphological transition to a nanorod. Next, we will investigate the changes in the type and area of crystallographic planes at the surface associated with the morphological transformation. The statistics-based atom-counting method has been applied to the atomic resolution distortion corrected images (Figs. 3(c,d)) by using StatSTEM²⁷. The atom-counting results of the nanodumbbell and nanorod, before and after heating respectively, are shown in Fig. 3(e,f). More details about the atom-counting procedure are provided in the Electronic Supplementary Information, Section S3 and Figs. S4-S7. The whole model is required for performing reliable MD simulations. Since only the right part of the nanodumbbell and nanorod has been imaged at atomic resolution, the shape of the remaining part of the nanodumbbell and nanorod will be approximated for the creation of a 3D model of the whole nanodumbbell and nanorod. The overall shape has been estimated from the low resolution image. The procedure to generate these initial 3D models is described in Section S4 of the Electronic Supplementary Information. In order to relax the initial 3D reconstructions, MD simulations have been performed. Although the atoms are allowed to move between projected

atomic columns, it is important to stress that the number of atoms per atomic column does not change more than the expected error for atom-counting on a particular column. The total number of atoms in the nanostructure remains the same during the relaxation. In Fig. S8 of the Electronic Supplementary Information, it is illustrated that the difference between the statistical atom-counts before and after relaxation is within the counting error and randomly distributed among the particle. The 3D atomic resolution reconstructions of the nanodumbbell and nanorod, before and after heating respectively, are shown in Fig. 4 along different directions. Along the direction of the electron beam additional, surface roughness is observed (Figs. 4(a) and (c), more details are provided in the Electronic Supplementary Information, Section S5). From the reconstructions, the surface facets can be clearly observed for the entire tip of the nanodumbbell and nanorod in Figs. 4(b) and (d). In Figs. 4(b) and (d), the direction of the incoming electron beam is indicated by a black arrow. In these figures, orange arrows indicate the width of the surface facets. These widths could already be observed from the projection images (Figs. 3(c) and (d)). On the other hand, yellow arrows indicate the *height* of the surface facets. This new information can only be obtained from the atomic resolution reconstructions, since the heights are parallel with the incoming electron beam in the projection images. The

3D atomic models suggest that the nanodumbbell and nanorod are mainly composed of $\{111\}$, $\{110\}$, and $\{100\}$ facets. The method is even sensitive enough to observe some of the higher index surfaces in between the lower index facets. Furthermore, the low index surface facets are seen to grow after heating the nanodumbbell. We observe part of this information from the silhouette in the high resolution projection images, however, the 3D atom-counting gives us additional information about the height of facets along the beam direction. Now, with the heights and the widths we directly observe the *area* of each facet of different index. This is directly comparable to other atomic resolution surface imaging techniques, such as field ion microscopy^{37–39}. However, in addition to the surface, we have the 3D structure suitable as a realistic input for computation materials science (e.g. density functional theory or MD calculations, simulated annealing,...).

Conclusions

In this paper, a recently developed atom-counting/energy-minimization method to reconstruct the atomic structure of nanoparticles in 3D from a single Z-contrast image has been validated against state-of-the-art compressive sensing electron tomography. When comparing the 3D atomic resolution reconstructions of both methods, an impressive agreement was found between the two methods. This indicates that the quantitative atom-counting results can be used as a reference to further improve electron tomography reconstruction algorithms. Such a synergistic combination of atom-counting and compressive sensing algorithms for electron tomography will enable to include quantitative prior information on the number of atoms during the reconstruction. Furthermore, the atom-counting/energy-minimization method opens the possibility for the study of beam-sensitive materials, 2D self-assembled structures¹⁹, and where *in situ* hardware makes tomography impossible. As an illustration, the surface facets of a Au nanodumbbell on an *in situ* heating holder were characterized. This heating experiment reveals a transition from a nanodumbbell to a nanorod with significant changes in facet areas. Such measurements are of critical importance for the characterization of nanomaterials and to study their physical behavior.

Acknowledgements

The authors gratefully acknowledge funding from the Research Foundation Flanders (FWO, Belgium) through project fundings (G.0374.13N, G.0369.15N, and G.0368.15N) and postdoctoral grants to T. Altantzis, A. De Backer, and B. Goris. S. Bals acknowledges financial support from the European Research Council (Starting Grant No. COLOURATOM 335078). Funding from the European Union Seventh Framework Programme under Grant Agreement 312483 - ESTEEM2 (Integrated Infrastructure Initiative-13) is acknowledged. The authors would also like to thank Luis Liz-Marzán, Marek Grzelczak, and Ana Sánchez-Iglesias for sample provision.

References

- 1 *Electron Tomography: Three-dimensional imaging with the transmission electron microscope*, ed. J. Frank, Plenum Press, New York and London, 1992.
- 2 P. A. Midgley and R. E. Dunin-Borkowski, *Nature Materials*, 2009, **8**, 271–280.
- 3 S. Van Aert, K. J. Batenburg, M. D. Rossell, R. Erni and G. Van Tendeloo, *Nature*, 2011, **470**, 374–377.
- 4 S. Bals, M. Casavola, M. A. van Huis, S. Van Aert, K. J. Batenburg, G. Van Tendeloo and D. Vanmaekelbergh, *Nano Letters*, 2011, **11**, 3420–3424.
- 5 B. Goris, S. Bals, W. Van den Broek, E. Carbo-Argibay, S. Gomez-Grana, L. M. Liz-Marzán and G. Van Tendeloo, *Nature Materials*, 2012, **11**, 930–935.
- 6 B. Goris, J. De Beenhouwer, A. De Backer, D. Zanaga, K. J. Batenburg, A. Sánchez-Iglesias, L. M. Liz-Marzán, S. Van Aert, S. Bals, J. Sijbers and G. Van Tendeloo, *Nano Letters*, 2015, **15**, 6996–7001.
- 7 R. Xu, C.-C. Chen, L. Wu, M. C. Scott, W. Theis, C. Ophus, M. Bartels, Y. Yang, H. Ramezani-Dakhel, M. R. Sawaya, H. Heinz, L. D. Marks, P. Ercius and J. Miao, *Nature Materials*, 2015, **14**, 1099–1103.
- 8 B. Goris, A. De Backer, S. Van Aert, S. Gómez-Graña, L. M. Liz-Marzán, G. Van Tendeloo and S. Bals, *Nano Letters*, 2013, **13**, 4236–4241.
- 9 K. H. W. van den Bos, A. De Backer, G. T. Martinez, N. Winckelmans, S. Bals, P. D. Nellist and S. Van Aert, *Physical Review Letters*, 2016, **116**, 246101.
- 10 Y. Yang, C.-C. Chen, M. C. Scott, C. Ophus, R. Xu, A. Pryor Jr., L. Wu, F. Sun, W. Theis, J. Zhou, M. Eisenbach, P. R. C. Kent, R. F. Sabirianov, H. Zeng, P. Ercius and J. Miao, *Nature*, 2017, **542**, 75–79.
- 11 S. Bals, S. Van Aert, C. P. Romero, K. Lauwaet, M. J. Van Bael, B. Schoeters, B. Partoens, E. Yücelen, P. Lievens and G. Van Tendeloo, *Nature Communications*, 2012, **3**, 897.
- 12 C. L. Jia, S. B. Mi, J. Barthel, D. W. Wang, R. E. Dunin-Borkowski, K. W. Urban and A. Thust, *Nature Materials*, 2014, **13**, 1044–1049.
- 13 L. Jones, K. E. MacArthur, V. T. Fauske, A. T. J. van Helvoort and P. D. Nellist, *Nano Letters*, 2014, **14**, 6336–6341.
- 14 M. Yu, A. B. Yankovich, A. Kaczmarowski, D. Morgan and P. M. Voyles, *ACS Nano*, 2016, **10**, 4031–4038.
- 15 J. M. LeBeau, S. D. Findlay, L. J. Allen and S. Stemmer, *Nano Letters*, 2010, **10**, 4405–4408.
- 16 A. De Backer, G. T. Martinez, A. Rosenauer and S. Van Aert, *Ultramicroscopy*, 2013, **134**, 23–33.
- 17 S. Van Aert, A. De Backer, G. T. Martinez, B. Goris, S. Bals and G. Van Tendeloo, *Physical Review B*, 2013, **87**, 064107.
- 18 S. Van Aert, A. De Backer, G. T. Martinez, A. J. den Dekker, D. Van Dyck, S. Bals and G. Van Tendeloo, *IUCrJ*, 2016, **3**, 71–83.
- 19 J. J. Geuchies, C. van Overbeek, W. H. Evers, B. Goris, A. De Backer, G. P. Gantapara, F. T. Rabouw, J. Hilhorst, J. L. Peters, O. Konovalov, A. V. Petukhov, M. Dijkstra, L. D. A. Siebbeles, S. Van Aert, S. Bals and D. Vanmaekelbergh, *Nature*, 2017, **542**, 75–79.

- ture Materials, 2016, **15**, 1248–1254.
- 20 C. Pecharrromán, J. Pérez-Juste, G. Mata-Osoro, L. M. Liz-Marzán and M. P., *Physical Review B*, 2008, **77**, 035418.
- 21 L. Y. Chang, A. S. Barnard, L. C. Gontard and R. E. Dunin-Borkowski, *Nano Letters*, 2010, **10**, 3073–3076.
- 22 H. Katz-Boon, C. J. Rossouw, M. Weyland, A. M. Funston, P. Mulvaney and J. Etheridge, *Nano Letters*, 2011, **11**, 273–278.
- 23 H. Katz-Boon, M. Walsh, C. Dwyer, P. Mulvaney, A. M. Funston and J. Etheridge, *Nano Letters*, 2015, **15**, 1635–1641.
- 24 M. Grzelczak, A. Sánchez-Iglesias, B. Rodríguez-González, J. Alvarez-Puebla, R. and Pérez-Juste and L. M. Liz-Marzán, *Advanced Functional Materials*, 2008, **18**, 3780–3786.
- 25 X. Sang and J. M. LeBeau, *Ultramicroscopy*, 2014, **138**, 28–35.
- 26 L. Jones, H. Yang, T. J. Pennycook, S. J. Marshall, S. Van Aert, N. D. Browning, M. R. Castell and P. D. Nellist, *Advanced Structural and Chemical Imaging*, 2015, **1**, 8.
- 27 A. De Backer, K. H. W. van den Bos, W. Van den Broek, J. Sijbers and S. Van Aert, *Ultramicroscopy*, 2016, **171**, 104–116.
- 28 S. Van Aert, J. Verbeeck, R. Erni, S. Bals, M. Luysberg, D. Van Dyck and G. Van Tendeloo, *Ultramicroscopy*, 2009, **109**, 1236–1244.
- 29 H. E. K. E. MacArthur, T. J. Pennycook, E. Okunishi, A. J. D'Alfonso, N. R. Lugg, L. J. Allen and P. D. a. Nellist, *Ultramicroscopy*, 2013, **133**, 109–119.
- 30 A. J. den Dekker, J. Gonnissen, A. De Backer, J. Sijbers and S. Van Aert, *Ultramicroscopy*, 2013, **134**, 34–43.
- 31 G. Grochola, P. S. Russo and I. K. Snook, *Journal of Chemical Physics*, 2005, **123**, 204719.
- 32 S. Plimpton, *Journal of Computational Physics*, 1995, **117**, 1–19.
- 33 W. M. Brown, P. Wang, S. J. Plimpton and A. N. Tharrington, *Computer Physics Communications*, 2011, **182**, 898–911.
- 34 A. De Backer, G. T. Martinez, K. E. MacArthur, L. Jones, A. Béché, P. D. Nellist and S. Van Aert, *Ultramicroscopy*, 2015, **151**, 56–61.
- 35 L. Jones, *IOP Conference Series: Materials Science and Engineering*, 2016, **109**, 012008.
- 36 A. De Backer, A. De wael, J. Gonnissen and S. Van Aert, *Ultramicroscopy*, 2015, **151**, 46–55.
- 37 E. W. Müller and K. Bahadur, *Physical Review*, 1956, **102**, 624–631.
- 38 E. W. Müller, *Journal of Applied Physics*, 1956, **27**, 474–476.
- 39 W. Lefebvre-Ulrikson, F. Vurpillot and X. Sauvage, *Atom Probe Tomography - Put Theory Into Practice*, Academic Press - Elsevier, 2016.

Electronic Supplementary Information:

Three-dimensional atomic models from a single Z-contrast image: verification by electron tomography and opportunities

A. De Backer,^a L. Jones,^b I. Lobato,^a T. Altantzis,^a B. Goris,^a P.D. Nellist,^b S. Bals,^{*a} and S. Van Aert^{*a}

^a Electron Microscopy for Materials Research (EMAT), University of Antwerp, Groenenborgerlaan 171, B-2020 Antwerp, Belgium

^b Department of Materials, University of Oxford, OX13PH Oxford, United Kingdom

* Corresponding authors: sandra.vanaert@uantwerpen.be, sara.bals@uantwerpen.be

S1 Drift correction

Prior to the statistics-based atom-counting method, the influence of sample drift during the acquisition of the experimental images can be post-compensated by using the known lattice proportions and angles between two planes at each specimen orientation. For example, for FCC gold in [001] orientation, the lattice proportion between the projected a - and b -direction equals 1 and the angle equals 90°. The procedure for drift compensation starts by finding all the atomic column positions from which the average lattice parameters and the angles between two planes are calculated. Then, the affine transformation T , which includes horizontal shear (α) and vertical scaling (β)

$$T \begin{bmatrix} x \\ y \end{bmatrix} = \begin{bmatrix} 1 & \alpha \\ 0 & \beta \end{bmatrix} \begin{bmatrix} x \\ y \end{bmatrix},$$

is obtained by minimizing the following cost function:

$$\chi^2 = \left(1 - \frac{r_{\text{th}}}{r_{\text{exp}}(\alpha, \beta)}\right)^2 + \left(1 - \frac{\theta_{\text{th}}}{\theta_{\text{exp}}(\alpha, \beta)}\right)^2$$

where r_{th} and r_{exp} are the theoretical and experimental lattice proportion, and θ_{th} and θ_{exp} are the theoretical and experimental angles between the two planes, respectively. The images are then drift compensated by applying this affine transform.

S2 Details of statistical atom-counting analysis Au nanorod

Using statistical parameter estimation theory, the scattering cross-sections can be quantified atomic column-by-atomic column by fitting an empirical imaging model to the experimental, drift corrected, images¹⁻⁵. This empirical imaging model consists of a sum of Gaussian peaks describing the atomic column intensities:

$$f_{kl}(\theta) = \zeta + \sum_{n=1}^N \eta_n \exp\left(\frac{-(x_k - \beta_{x_n})^2 - (y_l - \beta_{y_n})^2}{2\rho^2}\right) \quad (1)$$

where $\theta = (\beta_{x_1}, \dots, \beta_{x_N}, \beta_{y_1}, \dots, \beta_{y_N}, \rho, \eta_1, \dots, \eta_N, \zeta)^T$ are the unknown structure parameters with ρ being the width of the Gaussian peak, η_n the height of the n th Gaussian peak, β_{x_n} and β_{y_n} the x - and y -coordinate of the n th atomic column, respectively, and N the total number of analyzed atomic columns. The unknown parameters θ of the model are estimated in the least squares sense. The estimated scattering cross-sections $V_n = 2\pi\eta_n\rho^2$ then correspond to the volumes under the estimated Gaussian peaks. The fitted models for the drift corrected images of Figs. S1-S3(a) are shown in Figs. S1-S3(b). The models are in excellent agreement with the experimental data demonstrating their good quality. Next, the estimated scattering cross-sections can be visualized in a histogram as illustrated in Figs. S1-S3(c). Ideally, this histogram would consist of isolated components. However, due to a combination of instabilities of the microscope and sample, and noise effects, the components are smeared out. Therefore, the estimated scattering cross-sections are regarded as a statistical draw from an unknown probability distribution consisting of a superposition of Gaussian components, the

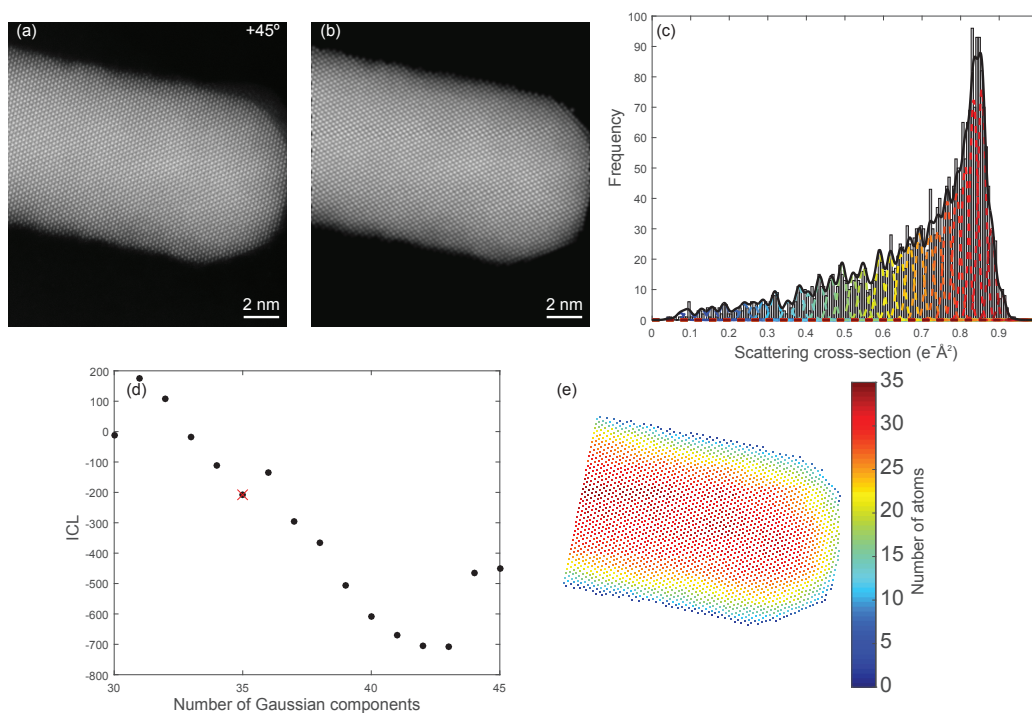


Fig. S1 Statistical atom-counting procedure for a Au nanorod along $[110]$ direction ($+45^\circ$) (a) Experimental drift corrected atomic resolution ADF STEM projection image, (b) Refined model, (c) Histogram of scattering cross-sections of the Au columns. The black curve shows the estimated mixture model; the individual components are shown as colored curves which correspond to the colors for the number of atoms in (e), (d) ICL criterion evaluated as a function of the number of Gaussian components in a mixture model, the selected minimum is indicated by a red cross, and (e) Number of atoms per column.

so-called Gaussian mixture model:

$$f_{\text{mix}}(V_n; \Psi_G) = \sum_{g=1}^G \pi_g \frac{1}{\sqrt{2\pi}\sigma} \exp\left(-\frac{(V_n - \mu_g)^2}{2\sigma^2}\right). \quad (2)$$

This model defines the probability that a specific scattering cross-section value V_n would be estimated for a particular atomic column n . The vector $\Psi_G = (\pi_1, \dots, \pi_{G-1}, \mu_1, \dots, \mu_G, \sigma)^T$ contains the unknown parameters π_g , μ_g , and σ being the mixing proportion of the g th component, the mean scattering cross-section of the g th component, and the width of the components, respectively. The parameters Ψ_G can be estimated from the experimental scattering cross-sections using the maximum likelihood estimator for a given number of components $G^{2,6-8}$. In practice, the value of G is unknown and has to be inferred from the available scattering cross-sections as well. The number of significant components, i.e. the model order G can be retrieved by evaluating the so-called integrated classification likelihood (ICL) criterion, which is shown in Figs. S1-S3(d). This order selection criterion balances the model fit against the model quality. Indeed the model fit will typically improve for increasing number of components and more details in the available set of scattering cross-sections will be described. However, for high-order models, these details are random and as a consequence the model quality will degrade with the model order. The estimated model order is given by the number of components for which ICL reaches a minimum, which is indicated by a red cross in Figs. S1-S3(d). In practice this minimum often corresponds to a local optimum rather than a global optimum². Figs. S1-S3(c) shows the estimated Gaussian mixture model. Based on this estimated probability distribution, the number of atoms can be identified by assigning each scattering cross-section to the component of the mixture model with the largest probability to generate this scattering cross-section. The atom-counts for every column of the nanorod are shown in Figs. S1-S3(e).

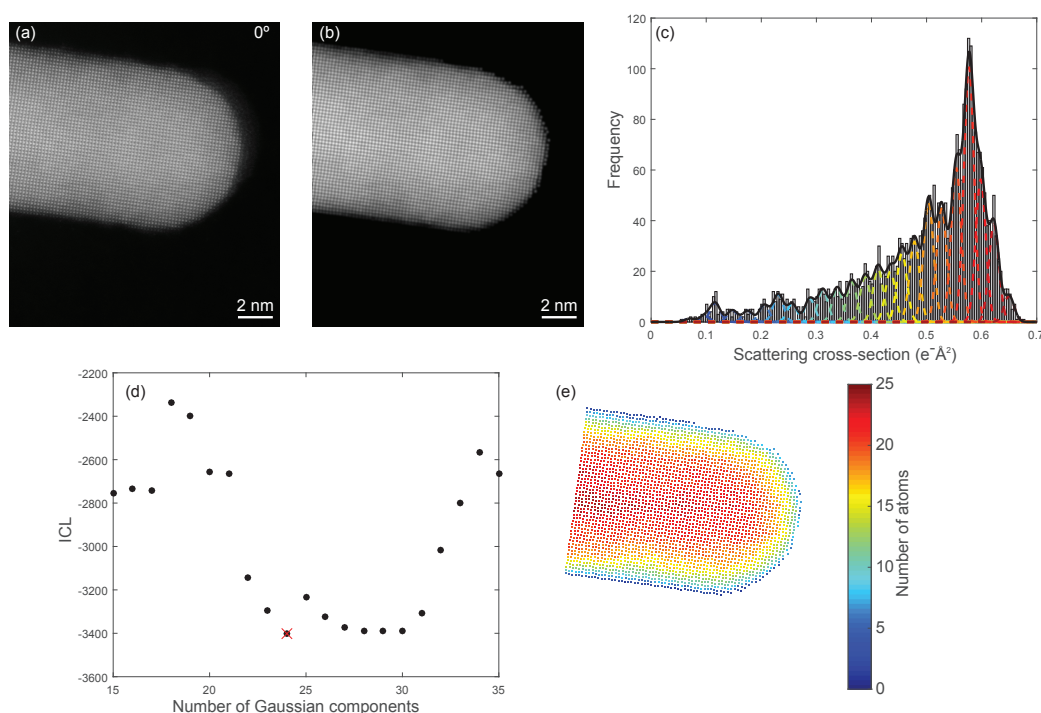


Fig. S2 Statistical atom-counting procedure for a Au nanorod in $[100]$ orientation (0°) (a) Experimental drift corrected atomic resolution ADF STEM projection image, (b) Refined model, (c) Histogram of scattering cross-sections of the Au columns. The black curve shows the estimated mixture model; the individual components are shown as colored curves which correspond to the colors for the number of atoms in (e), (d) ICL criterion evaluated as a function of the number of Gaussian components in a mixture model, the selected minimum is indicated by a red cross, and (e) Number of atoms per column.

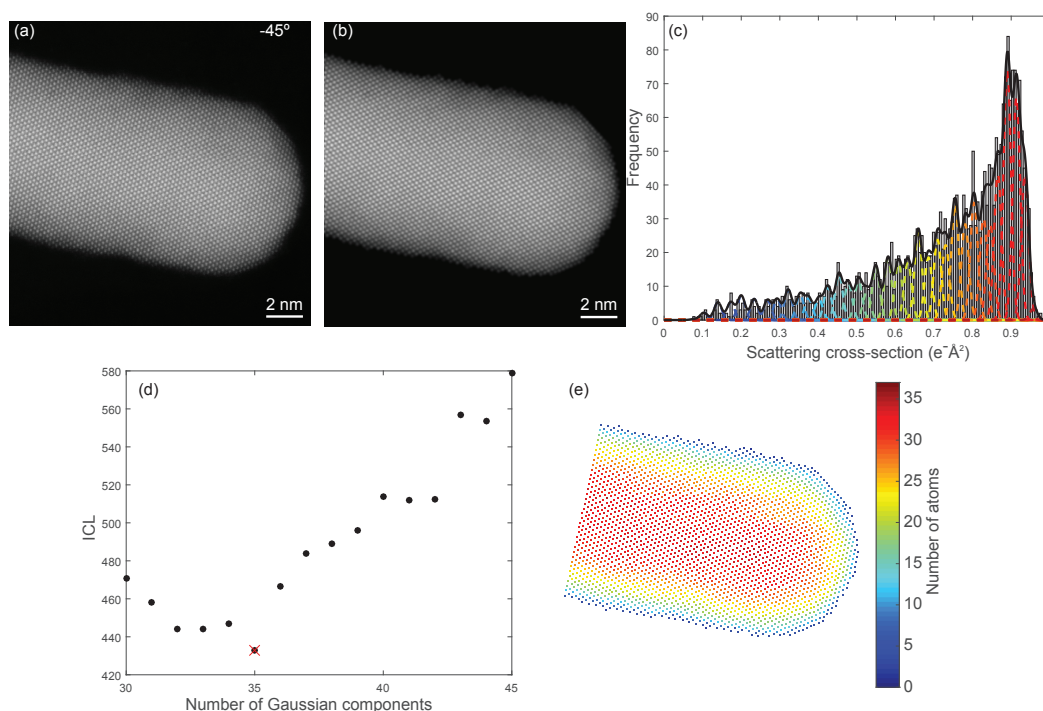


Fig. S3 Statistical atom-counting procedure for a Au nanorod in $[110]$ orientation (-45°) (a) Experimental drift corrected atomic resolution ADF STEM projection image, (b) Refined model, (c) Histogram of scattering cross-sections of the Au columns. The black curve shows the estimated mixture model; the individual components are shown as colored curves which correspond to the colors for the number of atoms in (e), (d) ICL criterion evaluated as a function of the number of Gaussian components in a mixture model, the selected minimum is indicated by a red cross, and (e) Number of atoms per column.

S3 Statistical atom-counting analysis for the heating experiment

For the heating experiment, atomic resolution images have been taken of the right part of the nanodumbbell and nanorod, before and after heating, respectively. These experimental images are shown in Figs. S4-S5(a). Since a very large number of atomic columns is present in these atomic resolution images a slightly adapted procedure as compared to the atom-counting of the previous Au rod has been applied. It has been illustrated by De Backer et al. that the number of atomic columns per component N/G in the Gaussian mixture model should be large enough². However, when N/G is too large for some components (corresponding to e.g. a high thickness) with respect to other components (with e.g. a small thickness), the number of components in the Gaussian mixture model will be overestimated. For the acquired images, there is such a disproportion for N/G for different thicknesses of the atomic columns: there are too many columns with a similar thickness in the thicker part of the nanoparticle. In order to circumvent this problem, the number of atomic columns that is used in the statistical atom-counting analysis is limited so that an optimal N/G value is obtained. These analyzes are shown in Figs. S4-S5. The (b) panels of these figures show the refined models of the experimental images, the (c) panels show the histograms of the scattering cross-sections of the Au columns with overlying the estimated mixture model and its individual components in color, the (d) panels show the ICL criterion evaluated as a function of the number of Gaussian components in the mixture model, and the (e) panels shown the number of atoms per column for the analyzed atomic columns. The locations of the components of the estimated Gaussian mixture models, which can be read out from the x -axis of the (d) panels, are plotted as a function of the corresponding number of atoms in Fig. S6. This figure shows mutual agreement between the analyzes before and after heating. These locations are used to extrapolate the atom-counting results to all the atomic columns of the of the atomic resolution images. The averaged locations of the 2 curves of Fig. S6 are used as a library for fitting the Gaussian mixture model with fixed locations for the scattering cross-sections of all the atomic columns present in the atomic resolution images. An overview of the final Gaussian mixture models for all the atomic columns of each atomic resolution image are shown in Fig. S7.

S4 Procedure to generate initial 3D models for the nanodumbbell and nanorod

In order to obtain a reliable molecular dynamics (MD) relaxation, 3D atomic models are needed of the whole nanodumbbell and nanorod. The procedure to generate the initial 3D models of the whole nanodumbbell and nanorod starts by finding the affine transformation, which includes scaling, rotation, and translation, of the atomic resolution STEM images of the right part of the nanorod with respect to the low resolution images of Fig. 3. Then these affine transformations have been applied to the atomic column positions obtained from the high resolution STEM images. An extra alignment and rotation over the atomic columns has been performed in order to be able to use the same grid for the whole nanorod. For the remaining left part of the nanodumbbell and nanorod, the atomic columns positions and corresponding number of atoms are unknown and need to be estimated. The atomic column positions, on the one hand, could be retrieved by thresholding the image and using a two-dimensional aligned grid. The number of atoms of this part, on the other hand, has been calculated by using the atom-counting results of the right parts of the nanodumbbell and nanorod. From these known parts, the intensity as a function of the number of atoms is known and fitted by a second order polynomial. This relation has been used to approximate the number of atoms of the remaining part of the nanodumbbell and nanorod. In this manner, the overall shape of these parts has been estimated from the low resolution image and can be used for the MD simulations.

S5 Surface roughness

The surface roughness in the reconstruction along the direction of the electron beam results from the limited precision of the atom-counts, introduced by the electron counting noise and scan noise present in the projection images^{2,9-11}. The statistics-based atom-counting method allows us to determine the percentage of all atomic columns in which the number of atoms is measured without error^{2,7}; for this experiment, this percentage equals 67%. Since the probability to measure atoms to have an error of ± 2 atoms equals almost zero here, 33% of all atomic columns are measured with an error of ± 1 .

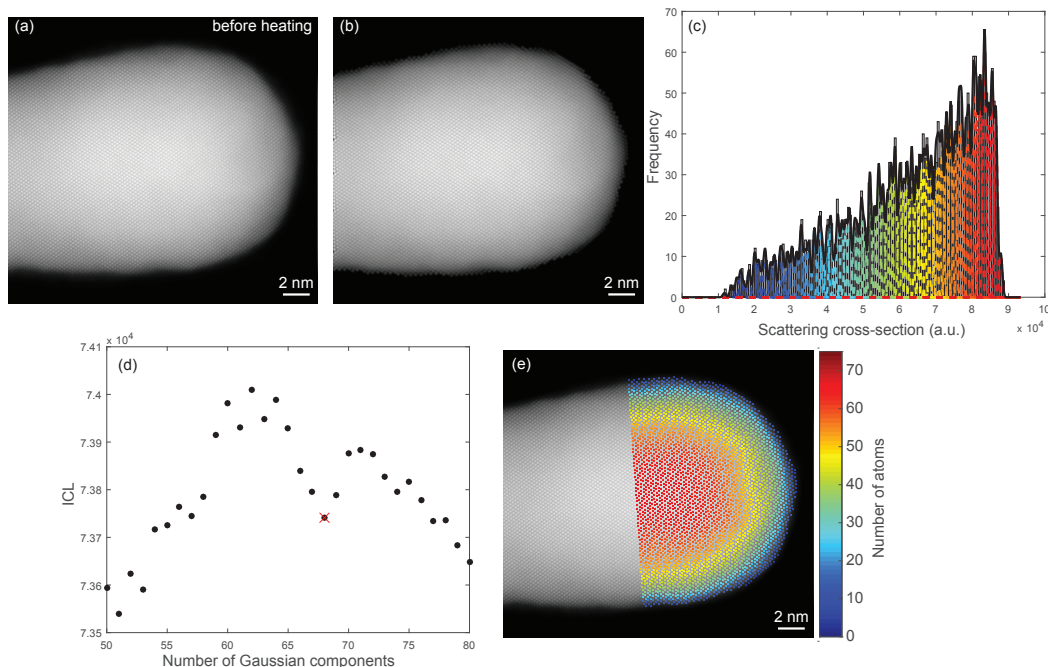


Fig. S4 Statistical atom-counting procedure for the Au nanodumbbell before heating (a) SmartAlign distortion corrected average of the experimental atomic resolution projection images along $[110]$ direction, (b) Refined model, (c) Histogram of scattering cross-sections of the Au columns. The black curve shows the estimated mixture model; the individual components are shown as colored curves which correspond to the colors for the number of atoms in (e), (d) ICL criterion evaluated as a function of the number of Gaussian components in a mixture model, the selected minimum is indicated by a red cross, and (e) Number of atoms per column.

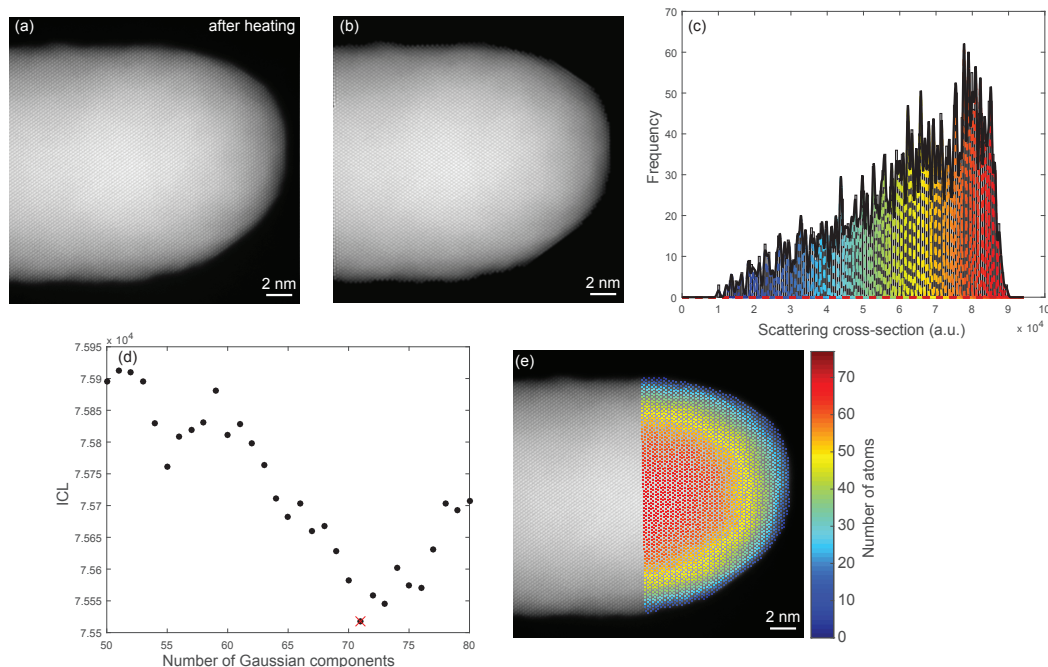


Fig. S5 Statistical atom-counting procedure for the Au nanorod after heating (a) SmartAlign distortion corrected average of the experimental atomic resolution projection images along $[110]$ direction, (b) Refined model, (c) Histogram of scattering cross-sections of the Au columns. The black curve shows the estimated mixture model; the individual components are shown as colored curves which correspond to the colors for the number of atoms in (e), (d) ICL criterion evaluated as a function of the number of Gaussian components in a mixture model, the selected minimum is indicated by a red cross, and (e) Number of atoms per column.

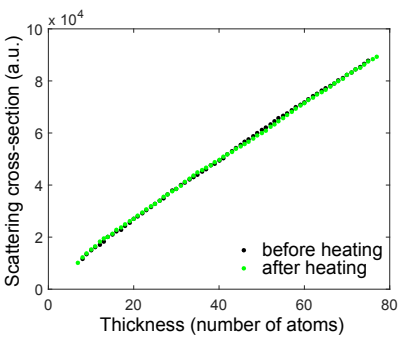


Fig. S6 Scattering cross-sections as a function of the thickness for the nanodumbbell and nanorod, before and after heating respectively.

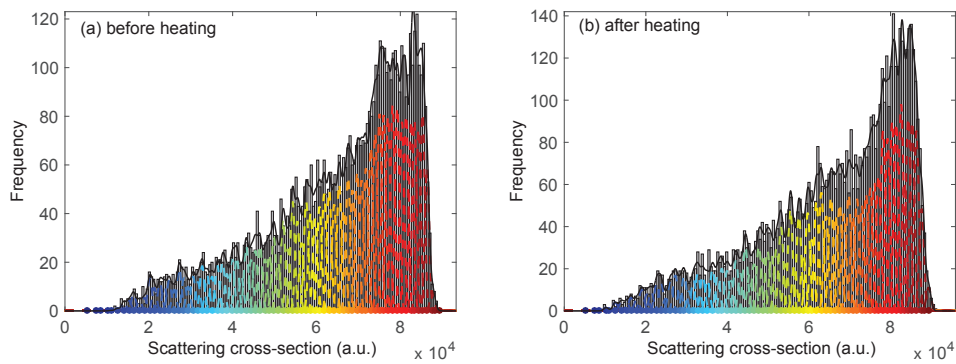


Fig. S7 Gaussian mixture models describing the distribution of the scattering cross-sections corresponding to all the projected atomic columns in the atomic resolution projection images for the nanodumbbell and nanorod, before and after heating, respectively.

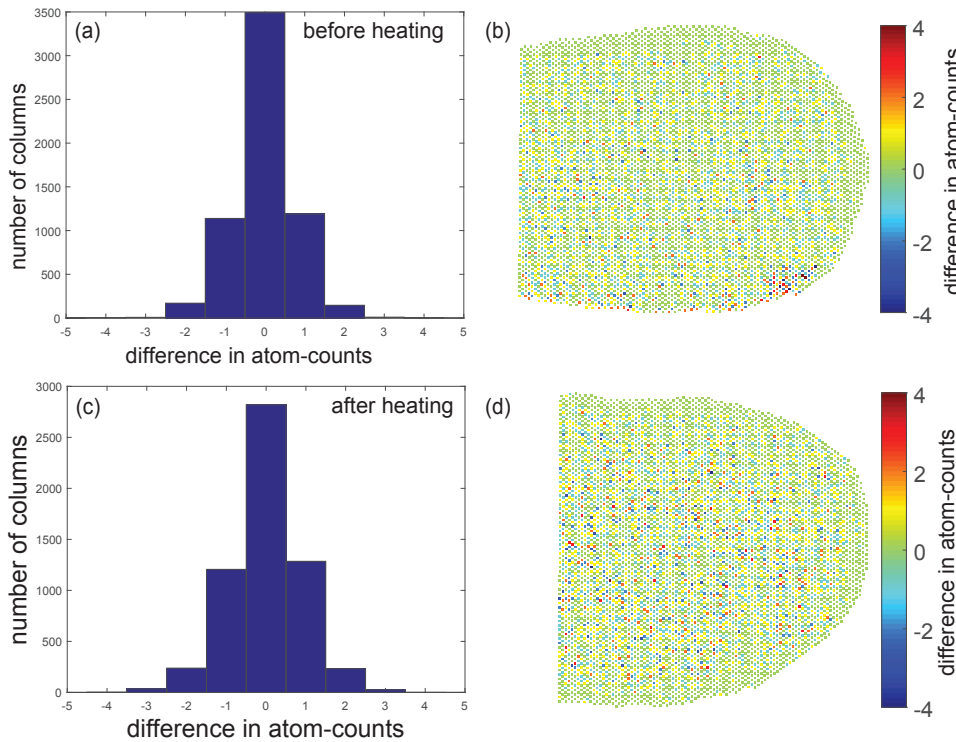


Fig. S8 Difference in atom-counts before and after relaxation per atomic column for the nanodumbbell and nanorod, before and after heating, respectively. The differences are presented in a histogram and an atomic column map. The differences are randomly distributed on the particle and are within the counting error.

References

- 1 S. Van Aert, J. Verbeeck, R. Erni, S. Bals, M. Luysberg, D. Van Dyck and G. Van Tendeloo, *Ultramicroscopy*, 2009, **109**, 1236–1244.
- 2 A. De Backer, G. T. Martinez, A. Rosenauer and S. Van Aert, *Ultramicroscopy*, 2013, **134**, 23–33.
- 3 A. J. den Dekker, J. Gonnissen, A. De Backer, J. Sijbers and S. Van Aert, *Ultramicroscopy*, 2013, **134**, 34–43.
- 4 S. Van Aert, A. De Backer, G. T. Martinez, A. J. den Dekker, D. Van Dyck, S. Bals and G. Van Tendeloo, *IUCrJ*, 2016, **3**, 71–83.
- 5 A. De Backer, K. H. W. van den Bos, W. Van den Broek, J. Sijbers and S. Van Aert, *Ultramicroscopy*, 2016, **171**, 104–116.
- 6 S. Van Aert, K. J. Batenburg, M. D. Rossell, R. Erni and G. Van Tendeloo, *Nature*, 2011, **470**, 374–377.
- 7 S. Van Aert, A. De Backer, G. T. Martinez, B. Goris, S. Bals and G. Van Tendeloo, *Physical Review B*, 2013, **87**, 064107.
- 8 G. McLachlan and D. Peel, *Finite Mixture Models*, John Wiley and Sons, inc., 2000.
- 9 A. De Backer, G. T. Martinez, K. E. MacArthur, L. Jones, A. Béché, P. D. Nellist and S. Van Aert, *Ultramicroscopy*, 2015, **151**, 56–61.
- 10 L. Jones, H. Yang, T. J. Pennycook, S. J. Marshall, S. Van Aert, N. D. Browning, M. R. Castell and P. D. Nellist, *Advanced Structural and Chemical Imaging*, 2015, **1**, 8.
- 11 L. Jones, *IOP Conference Series: Materials Science and Engineering*, 2016, **109**, 012008.